Localization of eigenfunctions in the stadium billiard

W. E. Bies*
Department of Physics, Harvard University, Cambridge, Massachusetts 02138

L. Kaplan
Institute for Nuclear Theory and Department of Physics, University of Washington, Seattle, Washington 98195

M. R. Haggerty
Department of Physics, Harvard University, Cambridge, Massachusetts 02138

E. J. Heller
Department of Physics and Department of Chemistry and Chemical Biology, Harvard University, Cambridge, Massachusetts 02138
(Received 25 April 2000; revised manuscript received 4 January 2001; published 22 May 2001)

We present a systematic survey of scarring and symmetry effects in the stadium billiard. The localization of individual eigenfunctions in Husimi phase space is studied first, and it is demonstrated that on average there is more localization than can be accounted for by random-matrix theory, even after removal of bouncing-ball states and visible scars. A major point of the paper is that symmetry considerations, including parity and time-reversal symmetries, enter to influence the total amount of localization. The properties of the local density of states are also investigated, as a function of phase space location. Aside from the bouncing-ball region of phase space, excess localization is found on short periodic orbits and along certain symmetry-related lines; the origin of all these sources of localization is discussed quantitatively and comparison is made with analytical predictions. Scarring is observed to be present in all the energy ranges considered. In light of our results, the excess localization in individual eigenstates is interpreted as being primarily due to symmetry effects.

DOI: 10.1103/PhysRevE.63.066214 PACS number(s): 05.45.Mt, 03.65.Sq

I. INTRODUCTION

According to scar theory, the quantum eigenfunctions of a classically chaotic dynamical system do not always look locally like random superpositions of plane waves with fixed energy, as predicted by Berry [1]; instead, many eigenfunctions display a concentration of amplitude around short unstable periodic orbits greater than that expected on the basis of random matrix theory fluctuations. The first examples of scars in the stadium billiard were presented by Heller [2], who also gave a semiclassical theory of scarring based on dynamics in the linearizable region around the periodic orbit (see also unpublished numerical work by McDonald [3]). Recent developments [4] have extended the theory of scars to the nonlinearizable regime, to include the effects of homoclinic recurrences at long times. Scarring is then seen to be a weak localization phenomenon coming from the short-time correlations associated with an unstable periodic orbit; in the energy domain, this means that a wave packet centered on the orbit may have nonrandom overlaps with the eigenstates of the system. Quantitative measures of scar strength have been developed and tested numerically [4,5].

In this paper we ask whether the localization caused by scarring on not-too-unstable (i.e., short) periodic orbits, and by atypical regions such as the ''bouncing ball'' [6–8] modes is adequate to predict measures of localization in eigenstates of chaotic systems. Quantitative numerical confirmation of scar theory [4,5] has been limited to discrete-time maps, and it would be desirable to study scarring quantitatively in the context of more realistic and experimentally realizable systems, such as the stadium (Bunimovich) billiard. In what follows we present a systematic study of eigenstate localization in the stadium billiard (see Ref. [9] for some other recent analyses of this system). In Sec. II, we first present the numerical method used to find the eigenstates. Then, in Sec. III, we study the localization properties of individual eigenstates, followed by an investigation in Sec. IV of the localization properties of the local density of states. We find evidence of scarring as a ubiquitous phenomenon, in all the energy ranges considered. We examine quantitative predictions of scarring strengths based on the classical structure around the unstable periodic orbits [4]. However, scar theory is not sufficient to explain all the observed localization. Symmetry effects, including the imprints of both time-reversal and parity symmetries, are ultimately found to dominate the excess wave function localization in the stadium.

II. METHOD

We study eigenstates of the time-independent Schrödinger equation in an infinite two-dimensional potential well having the shape of a stadium, taken here to consist of a square of side 2 with semicircular endcaps of radius 1. We use the plane wave method [10] to find states of even parity with respect to reflection about each of the two symmetry axes of the stadium. Since the eigenvalues are not known *a priori*, we search for them using the ''tension'' method: at each energy E we solve the linear system for the coefficients of the plane waves by singular-value decomposition, and then

*Electronic address: bies@blizzard.harvard.edu.

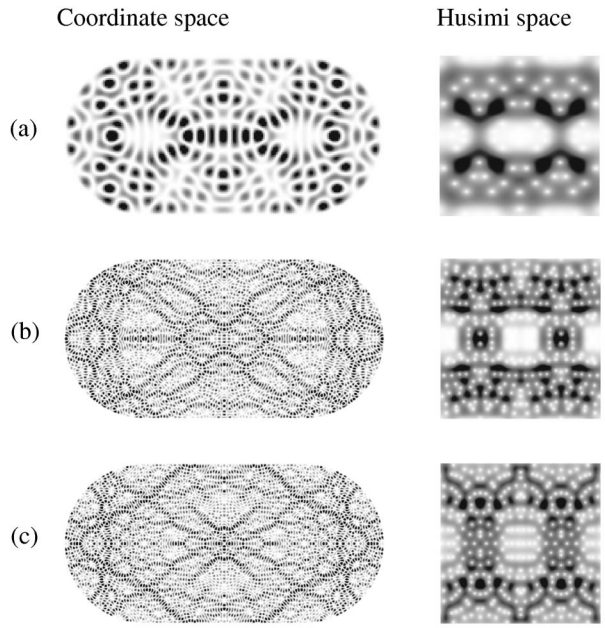

FIG. 1. Representative eigenfunctions of the stadium billiard in coordinate space (left) with x axis running from 0 to 4 and y axis running from -1 to 1, and in Husimi phase space (right) with distance q along the perimeter (horizontal axis) running clockwise from 0 (corresponding to the center of the upper straight segment) to $4+2\pi$ and tangential momentum (vertical axis) running from $-k$ to k, where k is the wave number of the eigenfunction. In the coordinate space plots, the gray level represents $|\psi|^2$. In the Husimi phase-space plots, white is high intensity and black low intensity. (a) $k=24.680$, (b) $k=100.787$, and (c) $k=105.608$, chosen to illustrate scarring along the bowtie and diamond orbits (cf. Table II).

compute the integral of $|\psi|^2$ along the boundary. If E is an eigenvalue the integral should vanish, to within numerical precision. In practice one finds sharp minima in the tension as a function of $k=\sqrt{E}$, which are identified with the eigenvalues. Using about eight points per wavelength along the boundary, we could reliably locate all eigenstates up to about $k=300$. Thus, we did not need the improvements to the plane-wave method developed by Li and Hu [11] and Vergini and Saraceno [12], although the methods described in these papers would be required to go to still higher values of k.

Lists of eigenstates of the even-even symmetry class in the three energy ranges of $k=20$ to 30, $k=100$ to 150, and $k=200$ to 225 were generated according to the method outlined above. Some examples are given in Fig. 1 of eigenfunctions $\Psi_n(x,y)$ in coordinate space.

Surface wave functions

Classically, one typically uses the boundary of the billiard as a Poincaré surface of section. The variables parametrizing the surface are q, the arclength along the boundary, and its conjugate momentum p, which is the component of momentum parallel to the wall (both positive in the clockwise sense). q is taken modulo the length $L\equiv 4+2\pi$ of the perimeter, while p is limited by energy considerations to $-k\leqslant p\leqslant k$. Then the classical billiard dynamics is reduced to a nonlinear one-bounce map, $(q',p')=M_{\rm cl}(q,p)$.

A natural way of reducing the quantum problem from two to one dimension is to characterize the Dirichlet eigenfunctions $\Psi_n(x,y)$, which are defined on the interior of the stadium, by their normal derivatives $\phi_n(q)$ on the boundary:

$$\langle q|n\rangle \equiv \phi_n(q) \propto \hat{\mathbf{n}}\cdot\boldsymbol{\nabla}\Psi_n(x,y). \tag{1}$$

We will study the properties of these *surface wave functions*. The wave functions are normalized according to the convention

$$\int\int dxdy|\Psi_n(x,y)|^2=1, \tag{2}$$

which is equivalent [13] to the following condition on the surface wave functions:

$$\frac{1}{2k^2}\int dq[\hat{\mathbf{n}}(q)\cdot\mathbf{r}(q)]|\phi_n(q)|^2=1, \tag{3}$$

where $\hat{\mathbf{n}}(q)$ is the unit normal at the position q along the boundary, and $\mathbf{r}(q)$ is the displacement vector from the center of the stadium to the position q.

The Husimi representation of a surface wave function $|n\rangle$ is given by its projection $|\langle q_0,p_0|n\rangle|^2$ onto test state Gaussians of the form

$$\langle q|q_0,p_0\rangle=\frac{1}{\sigma^{1/2}\pi^{1/4}}\exp\left[-\frac{(q-q_0)^2}{2\sigma^2}+ip_0(q-q_0)\right]. \tag{4}$$

The test Gaussian is centered at the point (q_0,p_0) in the boundary phase space. The parameter σ controls the aspect ratio of the Gaussian: its width in position is $\sigma/\sqrt{2}$ while its momentum width is $1/(\sigma\sqrt{2})$. To maintain a given aspect ratio of the Gaussian in phase space, σ must scale as $k^{-1/2}$. Here, we choose $\sigma=[(2+\pi)/k]^{1/2}$, which makes the aspect ratio unity in units where the full phase space on the billiard boundary is taken to be a square. Note that the wave functions are real in coordinate space but complex in phase space. Some example Husimi plots are given in Fig. 1.

III. IPR STATISTICS FOR INDIVIDUAL EIGENSTATES

We start by investigating the localization properties of individual eigenstates. As a measure of the degree of localization of the eigenstates in phase space, we use the mean squared value of the intensity, also known as the inverse participation ratio (IPR)

$$\mathcal{I}_n=\frac{(1/J)\sum_{j=1}^{J}|\langle q_j,p_j|n\rangle|^4}{\left[(1/J)\sum_{j=1}^{J}|\langle q_j,p_j|n\rangle|^2\right]^2}. \tag{5}$$

Here q_j and p_j range over the entire phase space as j varies on a sufficiently fine grid; the fineness J must scale at least linearly with the wave vector k. The range of momenta p_j covered is from $-k$ to $+k$ for a wave function with energy

k^2; outside this classically allowed region there is almost no wave function amplitude. The IPR $\mathcal{I}_n$ measures how much fluctuation across phase space there is in the nth eigenfunction. If $|\langle q_j,p_j|n\rangle|^2$ were completely uniform over phase space, $\mathcal{I}_n=1$. On the other hand, if all the intensity were concentrated entirely at one point j and was zero elsewhere, $\mathcal{I}_n$ would reach its maximal value J. [Of course, the uncertainty principle prevents $\mathcal{I}_n$ from ever becoming greater than the size of phase space in units of a Planck cell, i.e., $O(kL/2\pi)$.] Random-matrix theory (RMT) predicts a Porter-Thomas distribution of wave function intensities, yielding $\mathcal{I}_n=2$ (for complex wave functions), already larger than the naive classical expectation of 1.

A subtle point is that the wave function intensity $|\langle q_j,p_j|n\rangle|^2$, even when averaged over wave functions $|n\rangle$, is not uniform over the boundary phase space, being instead a non-trivial function of p_j. The mean wave function intensity can be determined from classical phase space arguments similar to those used in the derivation of Weyl's law. It depends on p for two reasons: (1) normal derivatives introduce a contribution of $p_\perp=k\sqrt{1-(p/k)^2}$ multiplying the coefficients of the plane waves [since the coefficients are squared, the resulting factor in the mean intensity is $k^2(1-(p/k)^2)$], and (2) there is a geometrical factor coming from the projection from the circle $k_\perp^2+p^2=k^2$ onto the boundary of the stadium. Because the plane waves are evenly distributed around the circle, there are more near $p=k$ than near $p=0$; the resulting geometrical factor is $[1-(p/k)^2]^{-1/2}$. Together, Eqs. (1) and (2) give

$$\langle|\langle q,p|n\rangle|^2\rangle_n\sim\sqrt{1-(p/k)^2}. \tag{6}$$

Therefore, even in the absence of quantum fluctuations, if the intensities for a wave function $|n\rangle$ were given simply by the mean value $|\langle q_j,p_j|n\rangle|^2=\sqrt{1-(p_j/k)^2}$ as in Eq. (6), we would obtain an IPR $\mathcal{I}_n$ of

$$\langle 1-(p/k)^2\rangle/\langle\sqrt{1-(p/k)^2}\rangle^2=\frac{32}{3\pi^2}\approx 1.080\,76, \tag{7}$$

independent of k. The averages $\langle\cdots\rangle$ here are of course taken over the classically allowed range of p: $-k<p<k$. If the intensity fluctuations around the smooth value $\sqrt{1-(p/k)^2}$ were instead given by a Porter-Thomas distribution, we would obtain $\mathcal{I}_n=1.08\times 2=2.16$ (since the smooth behavior and the Porter-Thomas fluctuations are independent of one another, the IPR contributions simply multiply).

We checked the mean wave-function intensity for the computed even-even states in the interval from $k=100$ to 110. It agrees well with Eq. (6), except at $p=0$ around the centers of the straight segments and the centers of the endcaps, where sharp peaks are seen. The peaks occur because only even-even states have been included in the analysis; since the odd states must vanish at the symmetry points, the even-even states compensate by having double the average intensity there. Apart from this, the agreement of the computed mean intensity with Eq. (6) indicates that we have included enough eigenfunctions in our analysis for each energy range.

TABLE I. Averages of the inverse participation ratios for the first 100 states in the three energy ranges starting at $k=20$, 100, and 200. Columns: (a) the k value at the beginning of the range; (b) the actual IPR; (c) the estimated fraction of phase space occupied by the bouncing-ball (BB) states in this range of k; (d) the predicted IPR when the bouncing-ball region is excluded; (e) the average actual IPR after the bouncing-ball states are omitted. Standard deviations are shown in parentheses. The large remaining discrepancy between (d) and (e) is mostly due to symmetry effects, as explained in the text.

(a) $k_{\min}$	(b) IPR numerical	(c) BB fraction of phase space	(d) IPR without BB RMT prediction	(e) IPR without BB numerical
20	3.67 (3.53)	13%	2.44	2.71 (0.62)
100	3.60 (3.33)	5.8%	2.29	2.70 (0.65)
200	3.08 (1.98)	4.1%	2.25	2.82 (0.80)

The average IPRs for the first 100 states in each energy regime are summarized in Table I.

The IPRs cluster around 3, with some much larger. The mean IPR is 3.67, 3.60, and 3.08 in the low-, medium-, and high-energy ranges, respectively, but with large standard deviations. Visual examination of the Husimi plots for states with the largest IPRs reveals that they correspond to bouncing-ball states. Since this phenomenon is well understood (and is associated with marginally stable periodic orbits), we remove this effect by eliminating the bouncing-ball states from the average [see column (e) of Table I].

The remaining states avoid the bouncing-ball region, causing their IPR to be increased by an amount that can be estimated. At $k\approx 20$, the bouncing-ball region occupies about 13% of phase space. Assuming the non-bouncing-ball states to vanish identically in that region, the random-matrix theory prediction for the average IPR without the bouncing-ball states becomes $2.16\times 1.13=2.44$. The size of the bouncing-ball region in phase space is energy-dependent (and must of course go to zero in the $k\to\infty$ limit, in order to satisfy the Shnirelman quantum ergodicity condition). As found by Tanner [7], the number of bouncing-ball states behaves asymptotically as $N_{\rm BB}(E)=0.36E^{3/4}$ and thus the density of bouncing-ball states, which is proportional to the area occupied by them in phase space, scales as $E^{-1/4}$ or $k^{-1/2}$. This scaling law, as well as the numerical prefactor, are in agreement with our numerical results. (We note that Bäcker *et al.* [6] find the same scaling law but a somewhat smaller prefactor when counting the bouncing-ball states. As explained in Ref. [6] part of the difference may be explained by the fact that Bäcker *et al.* do not count some states that live near the boundary of the bouncing-ball region. We are being conservative by eliminating all such states from our analysis; otherwise the observed discrepancy between calculated IPRs and RMT predictions would be even larger.) The adjusted RMT predictions are shown in column (d) of Table I.

As seen in Table I, the average IPRs with bouncing-ball states removed are still well above the random-matrix prediction in each energy range. The statistical uncertainty in the average IPR is about $1/\sqrt{100}\approx 0.1$ of the standard devia-

tion, or roughly 0.1, which is comparable to the differences in average IPR between different energy ranges. We do not see any trend toward the RMT predictions as k increases by a factor of 10.

Thus, we have uncovered systematic evidence of localization of eigenfunctions in the stadium billiard beyond what would be predicted on the basis of random-matrix theory. What is responsible for it? The next highest IPRs, after the bouncing-ball states, are for eigenfunctions visibly scarred along the periodic orbit that bounces horizontally between the centers of the endcaps. Thus, one might hypothesize that scarring along this and other periodic orbits is partly responsible for the excess localization. In the next section, however, we shall introduce a method that allows the excess localization to be identified with specific classical structures in phase space, and techniques to predict the amount of localization theoretically. We shall find that quantum symmetry effects cause most of the excess localization, while a secondary effect consists of combined scarring contributions from all of the short unstable periodic orbits.

IV. SPECTRAL LOCALIZATION

A. Introduction

The IPRs of individual eigenstates establish that there is indeed localization compared with the predictions of random-matrix theory. However, it does not permit the localization to be identified with specific structures in classical phase space because the IPR is an aggregate over all of phase space. But it is also possible to ask a complementary question, namely, how ergodic are the eigenstates at a given point in phase space as one varies the energy? To answer this question, we turn to the *local* IPR—a tool that provides a picture of the regions of phase space that are prone to intensity enhancement or depletion as one sweeps through an ensemble of eigenstates.

1. Definition

The local IPR (LIPR) $\mathcal{L}$ is the mean squared eigenstate intensity at point (q,p), averaged over a set of eigenstates [14]:

$$\mathcal{L}(q,p)=\frac{\frac{1}{N}\sum_{n=1}^{N}|\langle q,p|n\rangle|^4}{\left(\frac{1}{N}\sum_{n=1}^{N}|\langle q,p|n\rangle|^2\right)^2}, \tag{8}$$

where N is the number of eigenstates being summed over. Typically the sum is taken over eigenstates in a small energy range around some central value of k. The Gaussian wave packets $|q,p\rangle$ are adjusted to maintain constant aspect ratio in phase space as k changes [see discussion following Eq. (4)]; this keeps the classical dynamics fixed as the energy increases. The denominator in Eq. (8) depends analytically on p as in Eq. (6). Several LIPR pictures are shown in Fig. 2.

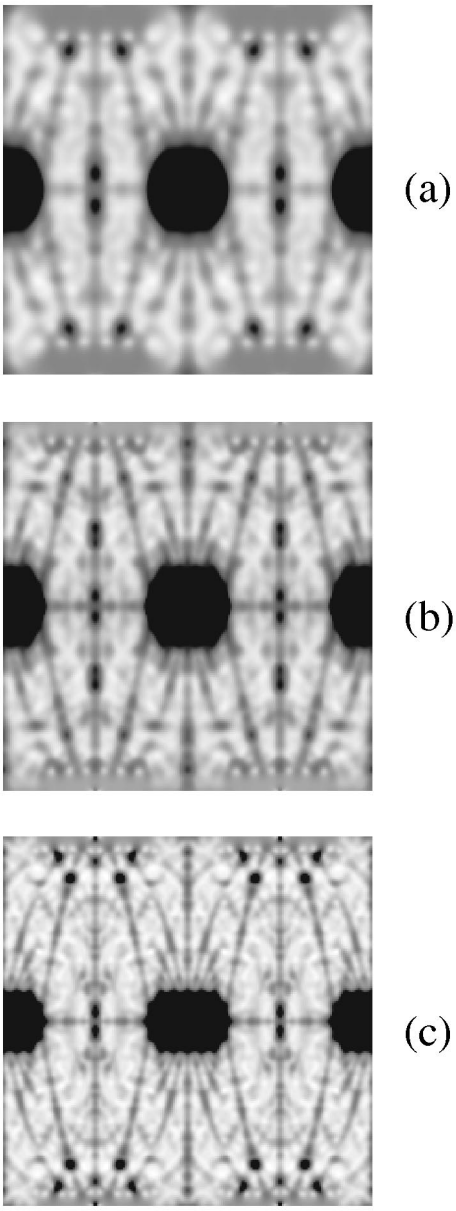

FIG. 2. LIPR [see Eq. (8)] in phase space as a function of q running horizontally from 0 to $4+2\pi$ and p/k running vertically from -1 to 1. The test-state width σ is chosen so that the test Gaussians have circular cross-sections when the figures are plotted with a square aspect ratio. Darker shading indicates higher values. (a) $k=50$ to 60, (b) $k=100$ to 150, and (c) $k=200$ to 225.

2. Intuitive description

The LIPR at the point (q,p) is a statistical property of the set of 'random' variables $\{\langle q,p|n\rangle : n=1\cdots N\}$. The second moment of this quantity [which appears in the denominator of Eq. (8)] is a smooth function of q and p, as was shown in Sec. III. The lowest nontrivial moment is the fourth moment, which appears in the numerator of Eq. (8). The LIPR, then, measures the nonuniformity of the local density of states at a (fixed) position in phase space.

We expect the LIPR $\mathcal{L}(q,p)$ to be a sensitive indicator of the presence of scarring, because a wave packet centered on

a periodic orbit has a local density of states that oscillates with energy [2]. Eigenstates in the peak of the oscillation will, on average, have enhanced overlaps with the test state, while eigenstates in the trough will have suppressed overlaps. This nonuniformity will cause the LIPR to have peaks near periodic orbits.

There is a useful interpretation of the LIPR—it is proportional to the long-time average of the probability that the wave packet $|q,p\rangle$, evolved in time, will return to its original location. A derivation and discussion of this interpretation are presented in Sec. IV E below.

Since the stadium is strongly chaotic, classical trajectories explore all of phase space (except for a set of measure zero). Therefore the classical return probability for long times is uniform, and the resulting naive classical prediction is that $\mathcal{L}=1$. This is indeed too naive.

Instead, the correct 'null hypothesis' for a chaotic system is that its eigenfunctions are random superpositions of plane waves [1]. Under this maximally random assumption, projections of wave functions on test states should follow a χ^2 distribution with one degree of freedom (if the eigenfunctions and test functions are real) or with two degrees of freedom (if they are complex). The corresponding predicted LIPRs are $\mathcal{L}=3$ or 2, respectively—already different from the naive classical prediction.

B. Introduction to pictures

In Fig. 2 we present the LIPR computed for even-even eigenstates in the wave number ranges $k=50$ to 60, 100 to 150, and 200 to 225. They display interesting and beautiful localization effects.

The horizontal axis of each picture is q, the position along the boundary, which runs from 0 to L. $q=0$ corresponds to the midpoint of one of the straight walls. The vertical axis is the component of momentum parallel to the boundary p/k, which runs from -1 to 1. The eightfold symmetry of these plots results from the two spatial reflection operations plus time-reversal symmetry. The LIPRs consistently show a very large enhancement in the bouncing-ball region, explainable by the bouncing-ball and near-bouncing-ball states present in the energy ranges considered. But in addition, there is localization in many other regions of phase space. There are very prominent straight lines of enhanced LIPR running along the lines of symmetry, and filamentary streaks running across other parts of phase space. There are also isolated spots at which the LIPR is unusually large.

Note that, although the details vary somewhat, the main localization features appear in the same positions in each energy range. This lack of $\hbar$ dependence suggests that the lines, streaks, and bright spots are all associated with semiclassical phenomena. Our main goal is to give a quantitative explanation for all of these effects. We would also like to understand the relative contributions of each semiclassical effect to the total average IPR enhancement found in Sec. III above.

C. Symmetry lines

What is the explanation for the streaks in the LIPR plots of Fig. 2? The most prominent streaks are shown schematically in Fig. 3. The streak labeled (1) in Fig. 3 corresponds to trajectories emerging from the center of the endcap. The streak labeled (2) corresponds to a family of orbits emerging from the center of the straight segment. Streak (3), which starts at small parallel momentum at the edge of the bouncing-ball region and extends to large momentum at the center of the endcap, corresponds to orbits that have a vertical segment in the endcap region. The box and the bowtie are the two most prominent periodic orbits in this family. The streak labeled (4) starts at small momentum at the center of the straight segment, curves up to larger momentum, and finally comes back down to zero momentum at the center of the endcap. It corresponds to orbits that pass through the center of the stadium. The most prominent periodic orbit in this family is the Z orbit. Finally, there is the horizontal line (5) going across the plot at zero momentum, corresponding to normal incidence on the billiard boundary. All of these families can be understood by considering time reversal and parity symmetry effects in combination with dynamics, as we will now see.

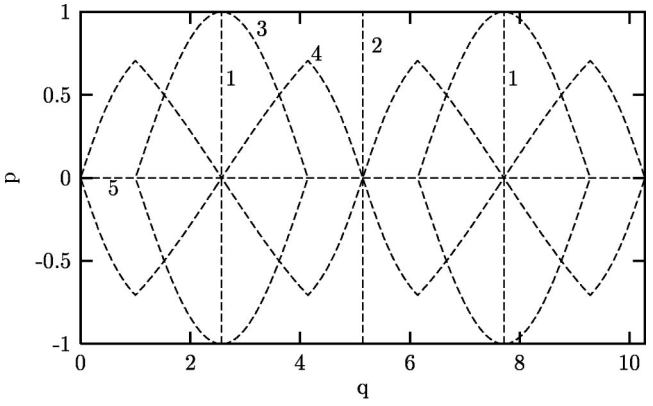

FIG. 3. Principal symmetry-related structures in phase space of the local inverse-participation ratio plotted in Fig. 2 and the average return probability plotted in Fig. 7. All symmetry lines are depicted schematically, labeled in the order in which they are described in the text.

1. Simple explanation

The intuitive reason for the symmetry lines is that the system, having time-reversal symmetry, has real eigenfunctions. However, the Gaussian test states [Eq. (4)] are intrinsically complex. Therefore the overlap $\langle q,p|n\rangle$ has both real and imaginary parts that, for most choices of q and p, are not trivially related to one another. Therefore the typical computed LIPR for the system is 2, characteristic of complex eigenfunctions. But in a sense the ''correct'' value $\mathcal{L}=3$ (characteristic of real eigenfunctions) is obscured by a nonideal choice of test states whose properties do not match those of the eigenstates.

However, due to the symmetry of the system, there are certain values of q and p for which the real and imaginary parts of $\langle q,p|n\rangle$ are not random and independent. For example, when $p=0$ (normal incidence to the wall), the test states and their projections $\langle q,p=0|n\rangle$ on the eigenstates become pure real and therefore near $p=0$ the LIPR increases

to 3. [This explains the symmetry line labeled (5) in Fig. 3.] Similarly, the eigenfunctions are symmetric about the centers of the straight walls, and therefore $\langle q=0,p|n\rangle$ is pure real and again the LIPR increases to 3. (Similarly for the centers of the endcaps.) This simple argument explains the straight symmetry lines (1), (2), and (5) that appear in the LIPR pictures. A rigorous derivation of their heights and widths will be given in the next section.

It is interesting to note that the same LIPR enhancements would be present if we had used eigenstates of other symmetry classes, or put eigenstates of all symmetry classes together. For example, for odd-odd eigenstates, the eigenfunctions are antisymmetric about the centers of the straight walls, and therefore $\langle q=0,p|n\rangle$ is pure imaginary, again giving a χ^2 distribution with one degree of freedom, and the enhancement $\mathcal{L}=3$.

A natural approach to desymmetrization would be to symmetrize the test wave packets with respect to time reversal symmetry, by taking their real or imaginary parts. We find, however, that such a simple procedure fails to eliminate all symmetry effects on the LIPR (and thus, also on the IPR).

2. Derivation

In this section we show how to compute the enhancement of the LIPR that appears near the symmetry lines of the system. We do this in order to verify the conclusions of the preceding simple arguments, and also to deduce important details such as the profiles and widths of the symmetry lines.

The derivation relies on the fact that the eigenfunctions are chosen to be real (in a coordinate basis), which can be done as a consequence of time-reversal symmetry. We denote time-reversal with T, an antiunitary operator. On the surface of section, $T|q,p\rangle=|q,-p\rangle$.

Furthermore, the eigenfunctions are symmetric or antisymmetric with respect to the reflections $x\to -x$ and $y\to -y$, which we will denote by the unitary operators R_x and R_y respectively. For simplicity in the following derivation we will consider the simpler case of a single reflection symmetry R about $q=0$.

It is not correct to model the eigenfunctions as uncorrelated Gaussian random variables, because their reflection symmetry correlates their values at different points. However, we can generate random wave functions $|n,\pm\rangle$ with positive $(+)$ or negative $(-)$ symmetry by taking completely random real wave functions $|n\rangle$ (with no symmetry) and projecting them onto the correct symmetry subspace:

$$|n,\pm\rangle=\frac{1}{\sqrt{2}}(|n\rangle\pm R|n\rangle). \tag{9}$$

To substitute into Eq. (8), we will need to compute $\langle q,p|n,\pm\rangle$. This quantity is complex, so we decompose it into two real random variables $\mu_\pm$ and $\nu_\pm$ as

$$\frac{1}{\sqrt{2}}[\langle\phi_{q,p}|n\rangle\pm\langle\phi_{q,p}|R|n\rangle]\equiv\mu_\pm+i\nu_\pm. \tag{10}$$

If $\mu_\pm$ and $\nu_\pm$ had the same variances and were uncorrelated, the LIPR would uniformly equal 2, like that of any Gaussian random process with two degrees of freedom. This null result would hold even if the variance depended on p and q, because the square of the variance appears both in the numerator and in the denominator of the definition of the LIPR.

However, in reality the symmetries cause the variances of the real and imaginary parts $\mu_\pm$ and $\nu_\pm$ to depend differently on phase space location. The effective number of degrees of freedom varies from two (when $\langle\mu_\pm^2\rangle=\langle\nu_\pm^2\rangle$) to one (when $\langle\mu_\pm^2\rangle\neq 0$, $\langle\nu_\pm^2\rangle=0$), and correspondingly the LIPR varies from 2 to 3.

In terms of the three quantities $\langle\mu_\pm^2\rangle$, $\langle\nu_\pm^2\rangle$, and $\langle\mu_\pm\nu_\pm\rangle$,

$$\langle|\mu_\pm+i\nu_\pm|^2\rangle=\langle\mu_\pm^2\rangle+\langle\nu_\pm^2\rangle, \tag{11}$$

while $\langle|\mu_\pm+i\nu_\pm|^4\rangle$ can be expanded and then contracted pairwise, giving

$$\langle|\mu_\pm+i\nu_\pm|^4\rangle=2(\langle\mu_\pm^2\rangle+\langle\nu_\pm^2\rangle)^2+(\langle\mu_\pm^2\rangle-\langle\nu_\pm^2\rangle)^2+4\langle\mu_\pm\nu_\pm\rangle^2. \tag{12}$$

The problem has been reduced to the computation of the required variances and correlations in Eq. (12).

Using $\langle q,p|n\rangle^*=\langle q,-p|n\rangle$ and $R|q,p\rangle=|-q,-p\rangle$, we obtain

$$\mu_\pm=\frac{1}{2\sqrt{2}}[\langle q,p|n\rangle+\langle q,-p|n\rangle\pm\langle -q,-p|n\rangle\pm\langle -q,p|n\rangle]$$

$$\nu_\pm=\frac{1}{2i\sqrt{2}}[\langle q,p|n\rangle-\langle q,-p|n\rangle\pm\langle -q,-p|n\rangle\mp\langle -q,p|n\rangle]. \tag{13}$$

Because $|n\rangle$ represents not a wave function but rather the projection of a wave function onto the surface of section, the closure relationship does not hold: $\Sigma_n|n\rangle\langle n|\neq\mathbb{1}$. But as explained above in Sec. IV A 1, it is still approximately true that

$$\sum_n|n\rangle\langle n|q,p\rangle\approx f(p)|q,p\rangle, \tag{14}$$

where $f(p)=f(-p)\sim\sqrt{1-(p/k)^2}$. It follows that

$$\begin{aligned}\langle\mu_\pm^2\rangle&=\frac{1}{8N}\sum_n[\langle q,p|n\rangle+\langle q,-p|n\rangle\pm\langle -q,-p|n\rangle\\&\quad\pm\langle -q,p|n\rangle][\langle n|q,p\rangle+\langle n|q,-p\rangle\pm\langle n|-q,-p\rangle\\&\quad\pm\langle n|-q,p\rangle],\\&=\frac{f(p)}{2N}[\langle q,p|q,p\rangle+\mathrm{Re}\langle q,p|q,-p\rangle\\&\quad\pm\mathrm{Re}\langle -q,p|-q,p\rangle\pm\langle q,p|-q,-p)];\end{aligned} \tag{15a}$$

the last line follows from $\langle q,-p|-q,p\rangle=\langle q,p|-q,-p\rangle$, which is real. The other correlations can be worked out similarly; the results are

$$\langle \nu_{\pm}^2\rangle=\frac{f(p)}{2N}[\langle q,p|q,p\rangle-\mathrm{Re}\langle q,p|q,-p\rangle\mp\mathrm{Re}\langle q,p|-q,p\rangle \pm\langle q,p|-q,-p\rangle] \tag{15b}$$

$$\langle \mu_{\pm}\nu_{\pm}\rangle=\frac{f(p)}{2N}[\mathrm{Im}\langle q,p|q,-p\rangle\pm\mathrm{Im}\langle q,p|-q,p\rangle]. \tag{15c}$$

3. Even and odd subsets vs whole set

At this point we must distinguish between two types of LIPR. First, one can evaluate the LIPR by averaging (in the numerator and the denominator) over only the even states (as done in this paper) or only the odd states. One then obtains

$$\mathcal{L}(q,p;\{|n,\pm\rangle\})=2+\frac{|\langle q,p|q,-p\rangle\pm\langle q,p|-q,p\rangle|^2}{(\langle q,p|q,p\rangle\pm\langle q,p|-q,-p\rangle)^2} =2+\frac{|\langle q,p|T|q,p\rangle\pm\langle q,p|RT|q,p\rangle|^2}{(\langle q,p|q,p\rangle\pm\langle q,p|R|q,p\rangle)^2}. \tag{16}$$

On the other hand, one can instead evaluate the LIPR by averaging over both the even and the odd states. In that case,

$$\mathcal{L}(q,p;\{|n,+\rangle\}\cup\{|n,-\rangle\}) =2+\frac{|\langle q,p|q,-p\rangle|^2+|\langle q,p|-q,p\rangle|^2}{\langle q,p|q,p\rangle|^2+\langle q,p|-q,-p\rangle^2} =2+\frac{|\langle q,p|T|q,p\rangle|^2+|\langle q,p|RT|q,p\rangle|^2}{\langle q,p|q,p\rangle^2+\langle q,p|R|q,p\rangle^2}. \tag{17}$$

The required matrix elements can be worked out from Eq. (4):

$$|\langle q,p|q',p'\rangle|=\exp\left[-\frac{(q-q')^2}{4\sigma^2}-\frac{\sigma^2(p-p')^2}{4}\right]. \tag{18}$$

The three LIPRs—Eq. (16) for even or odd symmetry and Eq. (17) for both symmetry classes put together—all can be shown to give results between 2 and 3. In fact, outside the region near $q=p=0$ the three results are identical; they all predict bright symmetry lines near $q=0$ (or near any q associated with a parity symmetry) of the form

$$\mathcal{L}(q,|p|\gg 1/\sigma)=2+e^{-2q^2/\sigma^2} \tag{19}$$

and bright symmetry lines near $p=0$ of the form

$$\mathcal{L}(|q|\gg\sigma,p)=2+e^{-2p^2\sigma^2}. \tag{20}$$

We note that the point $p=q=0$, near which the three LIPR definitions given above do not agree, will always be on a short periodic orbit (e.g., the horizontal bounce orbit of the stadium billiard), and so the behavior there in any case cannot be determined without taking dynamical scar effects into account (see Sec. IV D 2).

4. Curved symmetry lines

The curved streaks (3) and (4) in Fig. 3 also correspond to classical structures related to the system's symmetry. Consider first the streak labeled (3) in Fig. 3. It corresponds to trajectories with a vertical segment in the endcap region. In the desymmetrized quarter stadium, these trajectories are incident normally on the $y=0$ horizontal boundary, and a Gaussian test state with zero tangential momentum placed at the point of normal incidence $(q',p=0)$ would give rise to an enhanced LIPR $\mathcal{L}=3$, as for the zero-momentum line (5) above. Of course, this point of normal incidence exists only on the boundary of the *quarter* billiard. At other points along the same orbit, including points that also live on the boundary of the full stadium, a Gaussian with momentum aligned along the trajectory will be close to, but not exactly equal to, a time iterate of this zero-momentum Gaussian living on the $y=0$ boundary. The exact time iterate of this purely real Gaussian will in general be a Gaussian centered on the other periodic point (q,p) but with a (possibly complex) width σ somewhat different from that used in our test state. Thus, our test Gaussian at (q,p) will have significant overlap with an iterate of a purely real state at $(q',p=0)$ and result in an enhanced LIPR somewhere between 2 and 3. Very little wave packet rotation or stretching occurs during the short vertical trip between the $y=0$ line and the endcap; it is for this reason that the streak (3) is so strong. Further iterations of the dynamics will result in additional streaks of enhanced IPR; these, however, will be much weaker due to the additional stretching that makes a circular wave packet centered at these distant points less closely related to the evolved version of the $(q',p=0)$ real wave packet. All streaks in the LIPR plots that have not been explicitly identified in Fig. 3 may be explained as further iterates of symmetry lines we have discussed explicitly. The rather strong streak (4), associated with trajectories going through the center of the stadium, has a completely analogous explanation.

5. Quantitative contribution of the symmetry lines to the IPR

We can now estimate the contribution of the symmetry lines to the predicted average IPR. There are 12 strong, roughly vertical streaks [including the curved streaks (3) and (4)] in the region $p\neq 0$ and one horizontal streak at $p=0$. We assume temporarily the curved symmetry lines to have a central height near 3 and width of order σ just as for the $x=0$ symmetry line. Integrating the area under these streaks, assuming Eqs. (19) and (20) gives a predicted IPR from symmetry effects alone of 2.51 (in the energy range from $k=100$ to 150). The enhancement of the LIPR in the whispering-gallery region and in bright spots due to periodic orbits gives a contribution only of about 0.03, negligible in comparison to the symmetry effects. Since the bouncing-ball

region, which covers about 6% of phase space, is excluded from the above analysis, we should increase the prediction by 6% to 2.66 for the purpose of comparison with the numerical value of 2.70 ± 0.07. In the energy range from $k = 200$ to 225 the corresponding predicted IPR is 2.40, or 2.51 corrected for the bouncing-ball region, whereas the numerical value is 2.82 ± 0.08. Thus, it seems that inclusion of symmetry and bouncing-ball effects is sufficient to yield a quantitative understanding of much of the excess average IPR in Table I. Interestingly, scarring plays little role in the excess average IPR, but a very important role in understanding the phase-space structure.

D. Dynamics

In this section we will consider the LIPR for a system with no time-reversal symmetry, where the wave functions are complex instead of pure real, and the arguments of Sec. IV C concerning symmetry lines do not apply. In such a system the LIPR plot would be far more uniform, and most of the remaining structure would consist of isolated regions of enhanced LIPR, against a background of $\mathcal{L}=2$ (corresponding to the statistics of the square of a complex Gaussian variable). The streaks would be all gone, including the vertical parity-line streaks, which also depend on time-reversal symmetry for their existence. Thus in this section we study the effect of dynamics alone on the LIPR. First we give a general theory for computing the LIPR classically anywhere in phase space, and then we show an easier way to compute the LIPR in the neighborhood of a periodic orbit. In the process, we will also see how to treat the case of a periodic orbit that happens to lie on a symmetry line in a time-reversal invariant system.

1. Full dynamics treatment

First we show how to compute the enhancement of the LIPR due to the short-time dynamics of the system. Since we are considering the surface-of-section wave functions, the classical dynamics that is important is the classical Poincaré map $M_{\rm cl}$. However, since the effects we are seeking are quantum mechanical, we need to start from the corresponding *quantum* Poincaré map. For this we use the operator $M(k)$ that enters into the boundary integral method:

$$\langle q|M(k)|\phi\rangle \equiv \oint dq' K_{\rm ex}(q,q';k)\langle q'|\phi\rangle, \tag{21}$$

where the kernel is [13]

$$K_{\rm ex}(q,q';k) \equiv -\frac{ik}{2} H_1^{(1)}(k|\mathbf{r}(q)-\mathbf{r}(q')|) \times \hat{\mathbf{n}}(q)\cdot[\mathbf{r}(q)-\mathbf{r}(q')], \tag{22}$$

$\mathbf{r}(q)$ is a point on the billiard wall at arclength q, and $\hat{\mathbf{n}}(q)$ is the inward-pointing unit normal vector at q. Does $M(k)$ as defined generate the correct quantum dynamics? In a sense that is a philosophical question since the Poincaré map has no obvious exact quantum counterpart. However, $M(k)$ satisfies enough properties expected of a quantum Poincaré map that we shall use it:

(1) To within a semiclassical approximation it agrees with the semiclassical Poincaré map [13] (which is easier to define [15]).

(2) It is approximately unitary within a subspace whose dimension is given by the area of the Poincaré section in units of Planck's constant, and exponentially small outside of that subspace.

(3) If a boundary function $|n\rangle$ corresponds to a wave function that satisfies the boundary conditions at wave number $k=k_n$, then $|n\rangle$ is mapped onto itself under the action of $M(k)$:

$$M(k_n)|n\rangle = |n\rangle. \tag{23}$$

Indeed, this is the boundary integral method criterion for an eigenstate.

The following derivation should be considered suggestive rather than rigorous. For example, $M(k)$ is approximately unitary but it has eigenvalues both inside and outside the unit circle. This leads to difficulties analytically continuing it to the region of interest.

Given properties 2 and 3 above, it is clear that one crude way to find surface eigenstates of the system would be to apply $M(k)$ repeatedly to an arbitrary initial state $|\phi\rangle$ and average the results:

$$|n\rangle \propto \lim_{\epsilon\to 0^+} \sum_{j=0}^{\infty} [M(k_n)-\epsilon]^j |\phi\rangle = G(k_n)|\phi\rangle, \tag{24}$$

where

$$G(k) \equiv \lim_{\epsilon\to 0^+} \frac{1}{1-M(k)+\epsilon} \tag{25}$$

is similar to a Green's function. Since the component of $|\phi\rangle$ that projects onto $|n\rangle$ is unchanged by the action of $M(k_n)$, whereas the other components are multiplied by a complex phase, the only component that is not averaged out by the above procedure is the projection on $|n\rangle$.

Whenever k passes through an eigenvalue k_n, one of the eigenvalues $e^{i\alpha_n(k)}$ of $M(k)$ passes along the unit circle through 1 and $G(k)$ has a singularity. The singular part of G can be written schematically as

$$\frac{1}{\pi}\,\mathrm{Re}\; G(k) = \sum_n \frac{|n\rangle\,\delta(k-k_n)\langle n|}{|d\alpha_n(k)/dk|}. \tag{26}$$

The denominator gives the velocity of rotation of the nth eigenphase as it passes through 0. From Weyl's law, one can obtain an expression for the sum of eigenphase velocities (see, e.g., [16]):

$$\sum_n d\alpha_n/dk = kA, \tag{27}$$

where A is the billiard's area. Here the sum is over all eigenvalues of the scattering matrix. Now the dimensionality of this matrix is kL/π, where L is the perimeter of the billiard (the total number of wavelengths along the perimeter is $kL/2\pi$, so there is a total of kL/π modes that can live on the perimeter when one includes sines and cosines). Thus we can find the average phase velocity:

$$(kL/\pi)\langle d\alpha_n/dk\rangle = kA, \tag{28}$$

whence,

$$\langle d\alpha_n/dk\rangle = \pi A/L. \tag{29}$$

For a chaotic system, Eq. (29) holds not only in an average sense but also holds approximately for individual eigenphases. Therefore we take the eigenphase velocity outside of the summation, yielding the useful expression

$$\frac{A}{L}\mathrm{Re}\, G(k) \approx \sum_n |n\rangle \delta(k-k_n)\langle n|. \tag{30}$$

Note that the sum is over states of the full system, each with its distinct eigenvalue k_n.

It is a simple warm-up exercise to compute the denominator of the LIPR:

$$\begin{aligned}\sum_n |\langle q,p|n\rangle|^2 &= \sum_n \langle q,p|n\rangle\langle n|q,p\rangle \\ &= \sum_n \langle q,p|n\rangle \int dk\, \delta(k-k_n)\langle n|q,p\rangle \\ &= \frac{A}{L}\int dk\, \mathrm{Re}\langle q,p|G(k)|q,p\rangle \\ &= \frac{A}{L}\mathrm{Re}\int dk[\langle q,p|q,p\rangle + \langle q,p|M(k)|q,p\rangle \\ &\quad + \langle q,p|M^2(k)|q,p\rangle + \cdots]. \end{aligned} \tag{31}$$

Now note that $M(k)$ involves phases that vary rapidly with k; therefore only the first term in the brackets survives the integral over k. We are left with

$$\sum_n |\langle q,p|n\rangle|^2 \approx \frac{A\Delta k}{L}\langle q,p|q,p\rangle, \tag{32}$$

where Δk is the range of k over which the averaging is done.

To compute the fourth moment, we proceed as follows:

$$\begin{aligned}\sum_n |\langle q,p|n\rangle|^4 &= \sum_n \langle q,p|n\rangle\langle n|q,p\rangle\langle q,p|n\rangle\langle n|q,p\rangle \\ &= \sum_{n,m} \langle q,p|n\rangle \int dk\, \delta(k-k_n)\langle n|q,p\rangle \\ &\quad \times \langle q,p|m\rangle \int dk'\, \delta(k'-k_m)\langle m|q,p\rangle\, \delta_{nm}. \end{aligned} \tag{33}$$

Because of the $\delta(k-k_n)$ and $\delta(k'-k_m)$ factors, the Kronecker delta δ_{nm} may be replaced by $C\delta(k-k')$ where C is an undetermined constant with dimensions of momentum. Continuing, then, we have

$$\sum_n |\langle q,p|n\rangle|^4 = C\left(\frac{A}{L}\right)^2 \int dk dk'\, \mathrm{Re}\langle q,p|G(k)|q,p\rangle \times \mathrm{Re}\langle q,p|G(k')|q,p\rangle\, \delta(k-k') \tag{34}$$

$$= C\left(\frac{A}{L}\right)^2 \int dk [\mathrm{Re}\langle q,p|G(k)|q,p\rangle]^2 \tag{35}$$

$$= C\left(\frac{A}{L}\right)^2 \int dk \sum_{j,j'} \mathrm{Re}\langle q,p|M^j(k)|q,p\rangle \mathrm{Re}\langle q,p|M^{j'}(k)|q,p\rangle \tag{36}$$

$$\approx C\left(\frac{A}{L}\right)^2 \int dk \sum_j [\mathrm{Re}\langle q,p|M^j(k)|q,p\rangle]^2 \tag{37}$$

$$\approx \frac{C}{2}\left(\frac{A}{L}\right)^2 \int dk \sum_j |\langle q,p|M^j(k)|q,p\rangle|^2. \tag{38}$$

where in going to Eq. (37) we use the fact that for $j \neq j'$, the two phases in the integrand are approximately uncorrelated, and the integral averages to zero. Equation (38) (in obtaining which we note that for $j \neq 0$ the phase of $\langle q,p|M^j(k)|q,p\rangle$ is a rapidly changing function of k, and so may be regarded as random in the integration; the $j=0$ term is irrelevant in the infinite sum) may be interpreted as expressing the proportionality between the LIPR and the mean quantum return probability, averaged over *all* times. As a result of the reloading effect [4] this mean long-time return probability is proportional to the sum of the *short-time* recurrences, which may be cut off at the mixing time. The mixing time is defined as the time it takes for the classical dynamics to spread a given $\hbar$-sized cell throughout the entire phase space. In order of magnitude it is given by the one-bounce time T_B times the logarithm of the number of Planck-sized cells in the classical surface-of-section phase space, i.e., $j_{\mathrm{mix}} \sim T_{\mathrm{mix}}/T_B \sim \ln(kL)$.

Thus,

$$\sum_n |\langle q,p|n\rangle|^4 \approx \frac{C'}{2}\left(\frac{A}{L}\right)^2 \int dk \sum_{j=-j_{\mathrm{mix}}}^{j_{\mathrm{mix}}} |\langle q,p|M^j(k)|q,p\rangle|^2. \tag{39}$$

The constant of proportionality changes in going from Eq. (38) to Eq. (39), as is reflected in our change of notation from C to C'.

But at times shorter than the mixing time, the quantum map $M^j(k)$ can be approximated semiclassically in terms of the classical Poincaré map M^j_{cl} (which does not depend on k) times a phase that varies rapidly with k:

$$\langle q,p|M^j(k)|q,p\rangle \approx \langle q,p|M^j_{\mathrm{cl}}|q,p\rangle^{1/2} \exp(ik\ell_j), \tag{40}$$

where $|q,p)$ represents a classical Gaussian probability distribution centered at (q,p) (notationally distinguished from a

quantum wave function by the round brackets), $M_{\rm cl}^j$ is the classical Poincaré map iterated j times, and ℓ_j is the length of the corresponding classical trajectory. $(q,p|M_{\rm cl}^j|q,p)$ is the classical overlap of the original distribution with the j-times iterated distribution:

$$(q,p|M_{\rm cl}^j|q,p) \equiv \int dq'dp' P_{M_{\rm cl}^j(q,p)}(q',p') P_{q,p}(q',p'). \tag{41}$$

So finally we have

$$\sum_n |\langle q,p|n\rangle|^4 \approx \frac{C'}{2}\left(\frac{A}{L}\right)^2 \Delta k \sum_{j=-j_{\rm mix}}^{j_{\rm mix}} (q,p|M_{\rm cl}^j|q,p). \tag{42}$$

Combining Eq. (32) and Eq. (42) we obtain for the LIPR

$$\mathcal{L} = \frac{N\sum_n |\langle q,p|n\rangle|^4}{\left(\sum_n |\langle q,p|n\rangle|^2\right)^2} = \frac{C'N}{2\Delta k} \frac{\sum_{j=-j_{\rm mix}}^{j_{\rm mix}} (q,p|M_{\rm cl}^j|q,p)}{(q,p|q,p)}, \tag{43}$$

where the projections in both the numerator and in the denominator are classical. The constant C' can now be fixed by requiring that the LIPR, when evaluated far from any short periodic orbits (where scarring plays no role), should give the RMT value, which we call $\mathcal{L}(\mathrm{RMT})$. [As discussed above, $\mathcal{L}(\mathrm{RMT})=2$ in a system with no time-reversal symmetry; in the presence of time-reversal symmetry, $\mathcal{L}(\mathrm{RMT})$ reaches the value of 3 on certain symmetry lines. The LIPR contribution obtained from short-time dynamics must always be multiplied by the appropriate factor given by symmetry considerations; $\mathcal{L}(\mathrm{RMT})$ is inherently an effect arising from Heisenberg-time behavior and so must be considered separately from short-time contributions to the LIPR.]

Away from short periodic orbits there will be no recurrences, so only the $j=0$ term in the above sum contributes. Thus, we obtain the normalization constant $C' = (2\Delta k/N)\mathcal{L}(\mathrm{RMT})$ and finally

$$\mathcal{L}(q,p) = \mathcal{L}(\mathrm{RMT}) \frac{\sum_{j=-j_{\rm mix}}^{j_{\rm mix}} (q,p|M_{\rm cl}^j|q,p)}{(q,p|q,p)}. \tag{44}$$

2. Periodic orbits, linear theory

The dynamical description of the LIPR developed in the previous section provides a method of computing the LIPR classically, anywhere in phase space, by computing overlaps of classical Gaussian probability distributions with themselves iterated under the classical Poincaré map $M_{\rm cl}$. We found that the LIPR is enhanced when the short-time overlap is large. This of course is most dramatically the case in the neighborhood of a periodic orbit. In this section we show how to compute the LIPR in the neighborhood of a periodic orbit whose stable and unstable manifolds may have arbitrary orientation, using only the properties of that one orbit.

Figure 2 confirms the omnipresence of scarring in the eigenstates of the stadium billiard, as we now argue. In the general theory of scarring, a wave packet launched on a periodic orbit has a local density of states with a linear or short-time envelope (coming from dynamics linearized around the orbit) that is an oscillating function of energy [4]. The concentration of the local density of states in some energy regions and avoidance of others leads to an enhanced LIPR in Eq. (8). Thus the peaks in the LIPR plot in Fig. 2 at the positions of short periodic orbits must be attributed to scarring, even though for the most part the scars are too weak to be visible in coordinate-space plots of the wave functions, such as in Fig. 1. The scars are there in the sense of non-χ^2 variation of phase-space wave function intensity near the periodic orbits, as one scans through the eigenstates of the system. For typical scarred wave functions, the scarring will not be visible in coordinate space, even though the phase space intensity is greatly enhanced at the periodic points, as one can see in the Husimi plots.

In Fig. 4, we see that the distribution of wave function intensities on a periodic orbit indeed differs from the χ^2 distribution that would be expected on the basis of random-matrix theory. In Fig. 4(a) we show a histogram of wave function intensities measured using a Gaussian centered on the bowtie orbit for all states lying between $k=100$ and $k=150$. Because the bowtie orbit lies on a symmetry line, the random-matrix-theory prediction is a χ^2 distribution in one degree of freedom (for the 94% of eigenstates that are not bouncing-ball states). In the presence of scarring, the χ^2 distribution must be modulated by the linear spectral envelope corresponding to the periodic orbit, which can be obtained as the Fourier transform of the time-domain return amplitude for a wave packet initially centered on the orbit. For the bowtie orbit, the spectral envelope height varies from 0.4 to 2.3 with period in energy given by $2\pi/T$, where $T=2.6T_B$ is the period of the bowtie orbit. As a result of this modulation, there are many more very small and very large intensities in Fig. 4(a) than would be expected from the naive Porter-Thomas (RMT) picture. As plotted on a logarithmic scale, the effect is more pronounced for the large intensities, but also at low intensities we expect an enhancement by about 20%, which indeed is what is indicated by the data below $\langle I\rangle/10$. The amount of strong scarring observed is also quantitatively consistent with the predicted scarring corrections to random-matrix theory: for instance, the number of wave function intensities greater than ten times the mean is found to be 10 numerically, while the scar-corrected prediction is 13 ± 3 and the uncorrected random-matrix prediction is only 3 ± 3. These predictions were generated using a Monte Carlo simulation for peak heights chosen at random with the appropriate modulation.

At a generic point in phase space, not lying on a scar or on a symmetry line, we expect a χ^2 distribution in two degrees of freedom, and Fig. 4(b) shows the numerical distribution of wave function intensities at a generic point in phase space, in satisfactory agreement with the random-matrix-theory prediction for intensities greater than $\sim\langle I\rangle/10$ (without scarring corrections, since there is no scarring at a generic point in phase space, but with 6% of the intensities

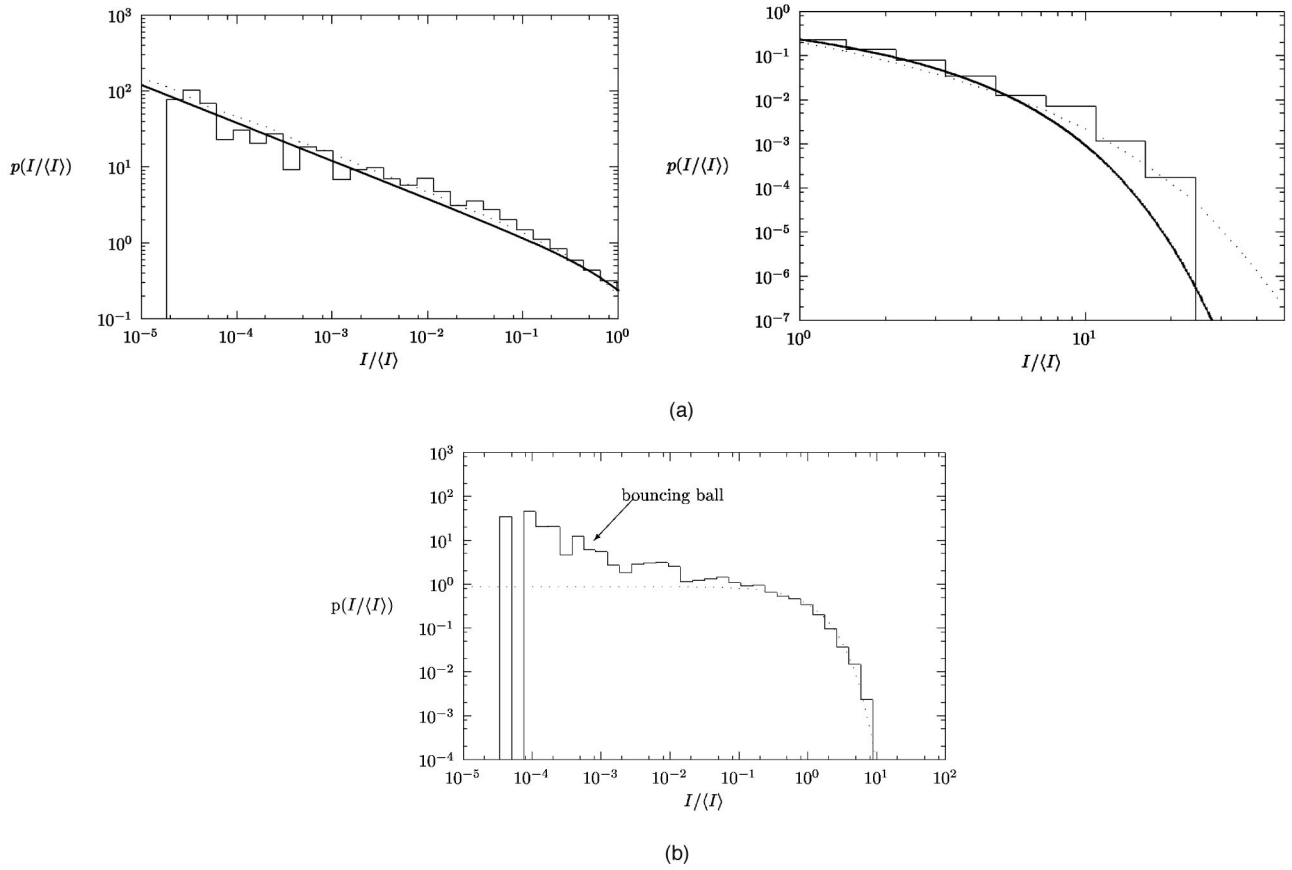

FIG. 4. Probability distribution of wave function intensities $I_n=|\langle q,p|n\rangle|^2$ for the 1746 energy levels between $k=100$ and 150. (a) For (q,p) situated on the bowtie orbit. Histogram, numerical distribution of wave function intensities; dotted line, scar-corrected prediction of random-matrix theory with one degree of freedom; solid line, random-matrix prediction, uncorrected for scarring. For purposes of illustration, the low-intensity part is shown in the figure on the left and the high-intensity tail on the right in a log-log plot. (b) Same as (a) but for (q,p) at a generic point in phase space, and the dotted line is now the random-matrix theory prediction for two degrees of freedom (without scar corrections, but adjusted for the 6% nearly vanishing intensities due to bouncing-ball states).

set to zero, namely, those corresponding to bouncing-ball states). The bouncing-ball states appear of course in the numerical data at intensities $I<\langle I\rangle/10$; the total area between the data and the curve in this intensity region indeed turns out to be 6%. Note the smaller number of very small and very large intensities as compared to the scarring case, Fig. 4(a). The two-degrees-of-freedom distribution also falls off much faster at large intensities than the one-degree-of-freedom prediction appropriate for a symmetry line.

We now turn to the calculation of the heights of the scarring peaks in Fig. 2 based on a linear expansion around periodic orbits. Consider the surface-of-section map in Birkhoff coordinates; we will be interested in the short-time linearized dynamics in the vicinity of a periodic orbit [2]. The stable and unstable invariant manifolds, defined as the locus of points that approach the periodic orbit under infinite iteration of the mapping forward or backward in time, respectively, will in general have an arbitrary orientation. We assume that we are far into the semiclassical regime, i.e., that k is large enough so that the Gaussian wave packet is well contained in the phase-space region where the linearized equations of motion are valid.

Due to the reloading effect mentioned in the preceding section (see also [4]) in which returning homoclinic orbits contribute in phase, the mean return probability for long times at a given periodic orbit, and hence the LIPR $\mathcal{L}$, which is proportional to the long-time return probability, will be equal to $\mathcal{L}$(RMT) times the short-time enhancement factor

$$S\equiv\sum_{j=-\infty}^{\infty}\int dqdpP_j(q,p)P_0(q,p)$$
$$=\sum_{j=-\infty}^{\infty}2\sqrt{\frac{\det A}{\det[A+(J^{-j})^TAJ^{-j}]}},\qquad(45)$$

where $P_0(q,p)$ is a classical Gaussian distribution centered on the periodic orbit and $P_j(q,p)$ is the same distribution evolved by j bounces. Strictly speaking, the sum in Eq. (45) should extend only over times short compared to the mixing time; however, this cutoff is irrelevant in the semiclassical limit $kL\gg1$ in which we are working. To show the second equality, let $x=(\delta q,\delta p)$ be the phase-space displacement relative to the periodic orbit and A be the quadratic form defining the initial Gaussian centered on the orbit,

$$P_0(x) = Ce^{-x^T Ax}, \tag{46}$$

with $\det A = 1$. We define J to be the Jacobian of $M_{\rm cl}$ at the periodic orbit; then

$$P_j(x) = C \exp[-x^T (J^{-j})^T A J^{-j} x] \tag{47}$$

and the overlap is indeed

$$\int dq dp P_j(q,p) P_0(q,p) = 2 \sqrt{\frac{\det A}{\det[A + (J^{-j})^T A J^{-j}]}} \tag{48}$$

(we see that using our normalization the overlap is unity at time $j=0$). Thus, the scar prediction of the LIPR peak heights at the periodic orbits—which takes into account the local stable and unstable directions at the periodic orbit, and not only the stability exponent—is $\mathcal{L}$ (RMT) multiplied by the short-time factor S.

Using a canonical transformation we may easily see that for any orientation of the manifolds there is an infinite one-parameter family of ''optimal'' Gaussian test states, all of which display maximum possible scarring in accordance with Eq. (45). S approaches unity for long or highly unstable orbits.

We have calculated S for the periodic orbits appearing in Fig. 5, and compare these theoretical predictions with the actual peak heights in Fig. 6.

To avoid having to deal explicitly with symmetry effects, we use the properties of the reduced orbits in the fundamental domain—one quarter of the stadium. Thus the periods of the most important orbits, as tabulated in Table II, range from $2T_B$ to $5T_B$ although their periods in the full stadium may be longer. As T increases beyond $T_H \approx 10T_B$, many of the short periodic orbits become incorporated into the streaks that dominate the IPR plots.

All quantities appearing in Fig. 6 are either predicted or actual values of $\mathcal{L}(q,p)/2$ at a periodic point (q,p). In other words, we have divided out by the RMT prediction $\mathcal{L}(\mathrm{RMT}) = 2$, which is relevant for all of phase space away from the symmetry lines. However, on the symmetry lines the RMT expectation is 3 rather than 2 (see Sec. IV C), so the theoretical values of S have been multiplied by 3/2 for those periodic points that do lie on symmetry lines. In fact, most of the points do lie on one or another symmetry line. With the inclusion of symmetry corrections, reasonable agreement is obtained, as can be seen in the scatter plots of the predicted versus calculated $\mathcal{L}/2$ peak intensities, Fig. 6; as shown in Fig. 6(c), the scatter is markedly worse when the symmetry corrections are omitted.

In order to appreciate the significance of these results, we should discuss the factors contributing to the uncertainty in the measured $\mathcal{L}/2$ values plotted in Fig. 6. There are two issues: first, there may be a nonintegral number of oscillations of the local density of states in the energy window considered. The size of this effect scales inversely with the number of scar oscillations in the energy window, and is only a few percent for the data presented in Fig. 6. A second, larger, source of error arises from the finite number of eigenvalues in the window. For random and independent fluctuations, the uncertainty coming from this effect scales as the square root of the mean level spacing divided by the size of the window. This is why the windows from $k=100$ to 150 and from $k=200$ to 225 were chosen to be as large as possible. A Monte Carlo simulation was done of random wavefunction intensities constrained by the ''linear'' spectral envelope: it suggests that the statistical uncertainty in the LIPRs should range from 5% to 8% (depending on the stability matrix J of the orbit in question) for periodic points on symmetry lines, and should be slightly smaller for those points that are not on any symmetry line. This level of fluctuation is roughly consistent with the dispersion in the scatter plots of Fig. 6, and does not alter the conclusion that S to-

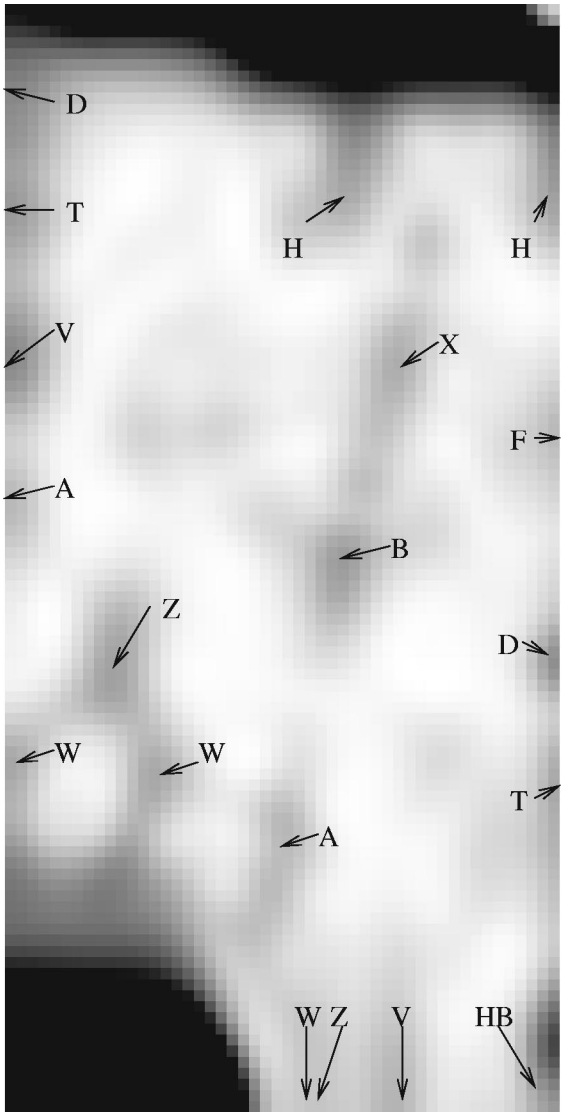

FIG. 5. Principal dynamics-related structures in phase space of the inverse-participation ratio plotted in Fig. 2 and the average return probability plotted in Fig. 7. The labeling is according to Table II labeling of scars on the principal short periodic orbits visible in Fig. 7(e), in an irreducible one-eighth region of phase space. The other regions of phase space are obtained by symmetry. The most prominent scarred orbits are *W*, *Z*, *D*, *B*, *X*, and *H*.

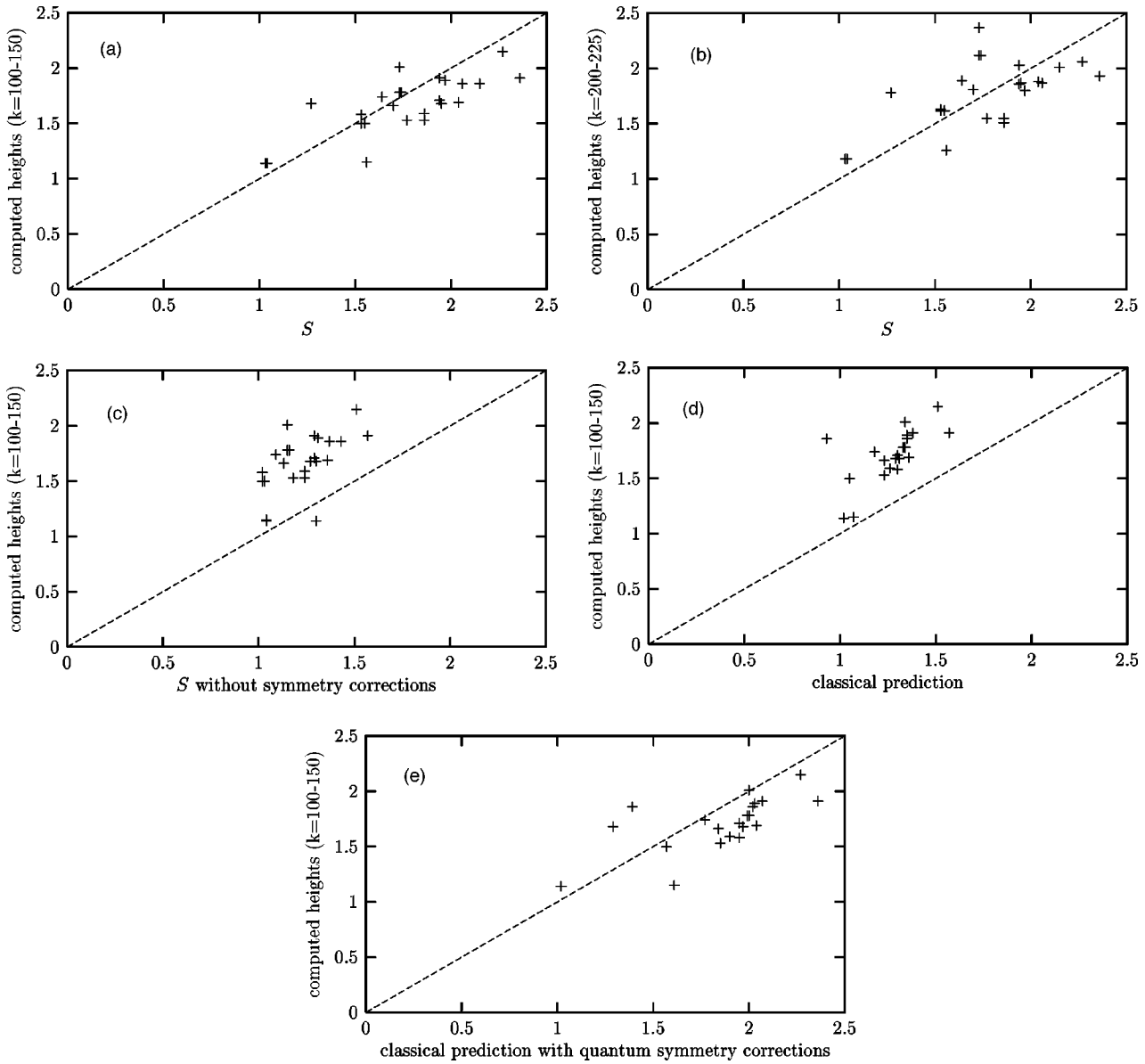

FIG. 6. Scatter plots of computed peak heights vs the linearized semiclassical prediction S and the brute-force semiclassical prediction. (a) Eigenfunctions ranging from $k=100$ to 150, symmetry corrections included in S; (b) $k=200$ to 225, symmetry corrections again included in S; (c) $k=100$ to 150, but symmetry corrections *not* included in S. Without symmetry corrections the agreement is much worse. (d) $k=100$ to 150 vs brute-force classical prediction without symmetry correction, and (e) with symmetry corrections included.

gether with symmetry factors is a good prediction of the peak heights. Thus, the symmetry lines emerge as essential to a quantitative understanding of the calculated LIPRs due to scarring. A final consideration supporting the validity of our symmetry analysis is the pattern of peak heights for the F orbit, on which periodic points F_1, F_3, and F_4 have a symmetry correction while F_2 and F_5 do not; the predicted peak heights for the points having symmetry corrections are about 50% percent higher than for the others, and this predicted pattern is reproduced in the calculated heights.

The brute-force classical calculation, at times large compared to T_B, goes beyond S to include the effects of nonlinear homoclinic recurrences, which add to the predicted peak height. For each periodic point, the returning probability for an initial Gaussian distribution centered at that point was integrated up to a cutoff time of $5T_B$, which was chosen to be large compared to T_B but smaller than the mixing time $T_{\mathrm{mix}} \approx 7T_B$, after which the returning probability approaches a constant per unit time independent of position in phase space. In the semiclassical limit, where strong, identifiable recurrences at times between the initial decay of the wave packet and the Heisenberg time can be neglected, the classical simulation converges to the quantum factor S. The classical simulation reproduces, as it must, one feature of the quantum data: the peak heights it predicts agree for points related by symmetry, namely, B_1 and B_2, Z_1 and Z_2, X_1 and X_2, A_1 and A_2, W_2 and W_4, H_2 and H_3, T_2 and T_3, and F_3 and F_4. In predicting the quantum heights, however, the brute-force classical calculation does no better than S and makes predictions that are systematically high (after includ-

TABLE II. Principal short periodic orbits appearing in Figs. 2 and 7. The initial coordinate q is the distance around the perimeter of the stadium measured clockwise from the center of the upper straight segment; the initial momentum p is positive in the clockwise sense. The lengths and periods are given for the desymmetrized stadium, which is relevant to our calculations.

Label	Description	q	p/k	Length (desymmetrized)	Period/T_B (desymmetrized)
HB	Horizontal bounce	2.5708	0	1	2.00
V	V shaped	0	0.70711	2	2.41
D	Diamond	2.5708	0.44721	2	2.24
B	Bowtie	1.5236	0.5	2	2.60
Z	Z shaped	0.5	−0.44721	3	3.24
X	Box	1.7854	0.70711	2	2.41
A	Accordion	0	0.5491	3	3.30
W	W-shaped	0	0.31623	4	4.16
H	Hexagon	2.5708	-0.86603	3	2.50
T	Triangle	0	0.83573	3	4.30
F	Fish	2.5708	0.6478	5	5.40

ing symmetry effects). In order to investigate the energy dependence of the classically predicted peak heights, the classical simulation was run both at $k=100$ and at $k=200$, the difference being in the size of the Gaussian as a fraction of the total phase space area. For almost all of the periodic orbits the results at the two energies agreed to within a few percent, which is of the same size as the discrepancy between the numerical quantum peak heights in the two energy ranges. This tells us that isolated, identifiable nonlinear recurrences beyond the initial decay of the wave packet away from the periodic orbit are not that important for computing the mean long-time return probability. Any such nonlinear effects would be strongly dependent on the size in phase space of the initial wave packet, i.e., on the wave number k.

The classical calculation for the average return probability can be performed anywhere in phase space, not only on the short periodic orbits considered in this section; see Sec. IV E 2 below. There we shall see that we obtain pictures similar to Fig. 2, but with more diffuse peaks and the onset of mixing for $T>T_{\mathrm{mix}}$.

E. Derivation as return probability

Finally, we explain the interpretation of the LIPR as the infinite-time average return probability, as in Eq. (49) below (where it is assumed that the energy window in the sums over n and n' is large enough to cover the energy scales present in the test state $|a\rangle$). In order to clarify what is happening in the infinite-time limit, it is useful to look first at finite times, and then let time tend to infinity. Thus we define the average return probability at time T for a wave packet $|\Psi_a\rangle$ to be [14]

$$
\begin{aligned}
P_{aa}(T) &= \frac{1}{2T}\int_{-T}^{T} dt |\langle \Psi_a | e^{-iHt} | \Psi_a \rangle|^2 \\
&= \frac{1}{2T}\int_{-T}^{T} dt \left| \sum_n \langle \Psi_a | n \rangle e^{-iE_n t} \langle n | \Psi_a \rangle \right|^2 \\
&= \frac{1}{2T}\sum_{nn'} \int_{-T}^{T} dt |\langle \Psi_a | n \rangle|^2 |\langle \Psi_a | n' \rangle|^2 e^{-i(E_n - E_{n'})t} \\
&= \sum_{nn'} \frac{\sin((E_n - E_{n'})T)}{(E_n - E_{n'})T} |\langle \Psi_a | n \rangle|^2 |\langle \Psi_a | n' \rangle|^2 . \qquad (49)
\end{aligned}
$$

In the limit as T tends to infinity,

$$
\frac{\sin((E_n - E_{n'})T)}{(E_n - E_{n'})T} \to \delta(E_n - E_{n'})
$$

and (in the case of a nondegenerate spectrum) we recover Eq. (8) up to an overall proportionality constant. The arbitrary state $|\Psi_a\rangle$ living in the interior of the stadium may be replaced by a Gaussian $|q,p\rangle$ living on the boundary if at the same time the eigenstates $|\Psi_n\rangle$ are replaced by their normal derivatives on the boundary, $|n\rangle$. For $T \ll T_B$ we should have $P_{aa}(T) \sim 1/T$; for intermediate times we expect classical behavior as long as $T<T_{\mathrm{mix}}$. The classical behavior will be computed directly below where, based on the time needed for a simulated classical ensemble to begin to spread evenly throughout phase space, we find $T_{\mathrm{mix}} \approx 7T_B$ at $k=100$; that it is so large may be attributed to intermittency due to bouncing-ball orbits. Finally for $T \gg T_H$, that is beyond the Heisenberg time where individual eigenstates are resolved [here, $T_H = 1/\Delta E = 1/(2k\Delta k) = 1/(2\times 100\times 0.05) = 0.1 = 10T_B$ at $k=100$], we should find that $P_{aa}(T)$ tends to the LIPR plot as shown in Fig. 2.

1. Finite-time return probability

The results for the time-dependent average return probability $P_{(q,p),(q,p)}(T)$ are given in Fig. 7, for the energy window at $k=100$. We are unable to study numerically the limit $T \ll T_B$ because of the finite number of eigenfunctions included in the sum in Eq. (49). At $T=T_B$, however, we see large amplitudes coming from the bouncing-ball and whispering-gallery regions of phase space, both of which are short-time classical effects. At $T=2T_B$ the horizontal-bounce orbit appears. By $T=3T_B$ several discrete peaks appear, and more of them are present at $T=4T_B$. These corre-

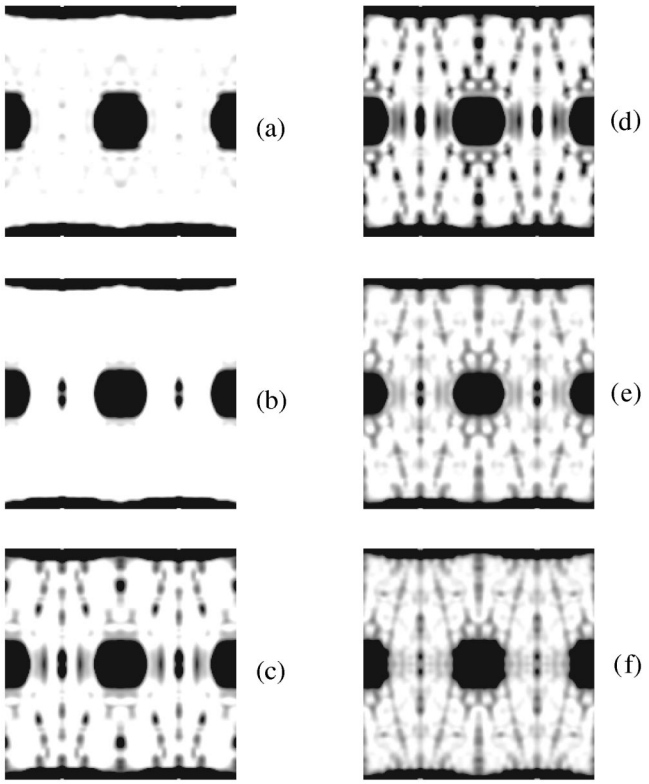

FIG. 7. Quantum-mechanical average-return probability $P_{aa}(T)$ as defined in Eq. (49), near $k=100$; q and p as before. (a) $T=T_B$, (b) $T=2T_B$, (c) $T=3T_B$, (d) $T=4T_B$, (e) $T=5T_B$, and (f) $T=10T_B$. Note the emergence of periodic orbits at $T=2T_B$ to $T=3T_B$. For $T=10T_B$ the figure is already beginning to resemble the LIPR plotted in Fig. 2(b).

spond to short periodic orbits of the classical dynamics in the desymmetrized quarter-stadium billiard. As T becomes as large as $5T_B$ and then $10T_B$ the finite-time average return probability indeed approaches the infinite-time LIPR. The nonuniform structure of the infinite-time return probability is a purely quantum mechanical effect, because according to classical mechanics the average return probability must become uniform for $T \gg T_{\mathrm{mix}}$.

Let us work with the data at $T=4T_B$, where the strong peaks are all present and readily distinguishable from the background [see Fig. 7(d)]. We identify these peaks with the short periodic orbits in Table II and Fig. 5.

2. Classical finite-time return probability

The persistence to long times of short-time classical information is a remarkable property of the quantum mechanics. Classically, we would expect the recurrences to be washed out at times large compared to the mixing time. Indeed, we have computed a classical analog to the time-dependent average return probability from Eq. (44). As shown in Fig. 8, by $T=10T_B$ all of the periodic orbits seen in the quantum calculation are present, although the peaks are more diffuse classically, but by $20T_B$ the classical picture is beginning to be uniformly distributed throughout phase space, losing memory of the short-time behavior. Quantum

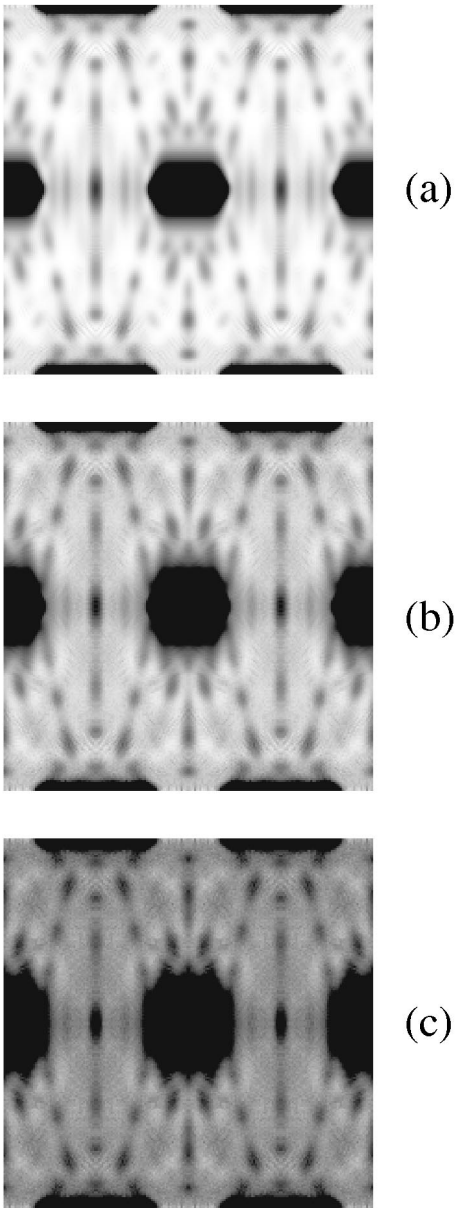

FIG. 8. Results of a classical calculation of the return probability vs time, q running horizontally from 0 to $4+2\pi$ and p vertically from -1 to 1. Initial Gaussians were chosen with $\sigma^2=0.05$, corresponding to a spread in position space of 0.2 out of $4+2\pi$, or 2% of the perimeter. All of the major periodic orbits are present here as short-time recurrences. (a) $T=5T_B$, (b) $T=10T_B$, (c) $T=20T_B$.

mechanically, of course, the peaks do not become washed out at long times and instead persist in the infinite-time limit, Fig. 2.

V. CONCLUSION

The advantage of the approach implemented in Sec. IV is that all of the scars can be observed simultaneously in the plot of inverse participation ratio as a function of phase-space location. Although scars are associated with the classical structure of unstable periodic orbits, the persistence to long times of an excess in the average return probability is a

purely quantum mechanical phenomenon. The brightnesses of the peaks in the LIPR plot can be predicted semiclassically with some success (to an accuracy of 10– 15 %), the size of the deviations being roughly consistent with expected statistical fluctuations. More precise comparison with the scar theory predictions would require producing a greatly increased set of eigenstates: this could be done by going to higher energies or (with far less computational expense) by using an ensemble of chaotic systems with a given unstable orbit kept fixed [4]. The predictions of brightnesses based on exact classical phase-space evolution at the end of Sec. IV were no more successful than those based on linearized behavior around the periodic orbit.

Most of the extra localization of individual eigenfunctions in Husimi phase space, over and above Gaussian random fluctuations, may be satisfactorily accounted for by quantum symmetry effects. Scarring is also seen to be present based on an analysis of the spectra of wave packets located on short periodic orbits. Symmetry effects on the overall mean IPR scale as $O(\sqrt{\hbar})$ [i.e., $O(\sqrt{1/k})$], while the effect of scarring on the overall mean IPR scales as $O(\hbar)$ [i.e., $O(1/k)$]. The reason, for the symmetry effects, is that the widths in position and momentum of the test-state Gaussian scale as $\sigma \sim \sqrt{\hbar}$, setting the width of the symmetry lines [Eqs. (19) and (20)], while the length of the symmetry-enhanced lines is $\hbar$ independent. Thus, the total fraction of phase space covered by the symmetry lines scales as $\sqrt{\hbar}$. The scar effect, on the other hand, is significant for those phase-space Gaussian wave packets that have large intensity on the periodic orbit [17], and the fraction of such Gaussians goes as the area of the Gaussian; i.e., as $\sqrt{\hbar} \times \sqrt{\hbar} = \hbar$. We note that although the size of both these effects on the overall wave function IPR is expected to go to zero in the semiclassical limit (because periodic orbits and symmetry lines both affect a smaller and small fraction of phase space surrounding them, in the $\hbar \to 0$ limit), the local IPR either on a symmetry line or on a periodic orbit is $\hbar$ independent. Thus, as measured using the local IPR, deviations from naive RMT predictions persist to arbitrarily high energies and do not decay in the semiclassical limit. As for other possible kinds of eigenfunction localization, not associated with the short periodic orbits of the system or with symmetry lines, their explanation remains an open question.

ACKNOWLEDGMENT

This research was supported by the National Science Foundation under Grant No. CHE-9610501.

[1] M. V. Berry, in *Chaotic Behaviour of Deterministic Systems*, edited by G. Iooss, R. Helleman, and R. Stora (North-Holland, Amsterdam, 1983), p. 171.
[2] E. J. Heller, Phys. Rev. Lett. **53**, 1515 (1984).
[3] S. W. McDonald, Ph.D. thesis, University of California at Berkeley (1983).
[4] L. Kaplan and E. J. Heller, Annals of Physics **264**, 171 (1998); L. Kaplan, Phys. Rev. Lett. **80**, 2582 (1998); see also the review: L. Kaplan, Nonlinearity **12**, R1 (1999), and references therein.
[5] L. Kaplan and E. J. Heller, Phys. Rev. E **59**, 6609 (1999).
[6] A. Bäcker, R. Schubert, and P. Stifter, J. Phys. A **30**, 6783 (1997); see also P. W. O'Connor and E. J. Heller, Phys. Rev. Lett. **61**, 2288 (1989).
[7] G. Tanner, J. Phys. A **30**, 2863 (1997).
[8] M. Sieber, U. Smilansky, S. C. Creagh, and R. G. Littlejohn, J. Phys. A **26**, 6217 (1993); J. S. Espinoza Ortiz and A. M. Ozorio de Almeida, *ibid.* **30**, 7301 (1997).
[9] A. Bäcker and R. Schubert, J. Phys. A **32**, 4795 (1999); G. Casati and T. Prosen, Phys. Rev. E **59**, R2516 (1999); B. Eckhardt, S. Fishman, J. Keating, O. Agam, J. Main, and K. Muller, Phys. Rev. E **52**, 5893 (1995).
[10] E. J. Heller, in *Chaos and Quantum Physics, Proceedings of the Les Houches Summer School, (Les Houches Session 52)*, edited by M. J. Giannoni, A. Voros, and J. Zinn-Justin (Elsevier, North-Holland, Amsterdam, 1991), p. 602.
[11] B. Li and B. Hu, J. Phys. A **31**, 483 (1998); B. Li, Phys. Rev. E **55**, 5376 (1997).
[12] E. Vergini and M. Saraceno, Phys. Rev. E **52**, 2204 (1995); F. P. Simonotti, E. Vergini, and M. Saraceno, *ibid.* **56**, 3859 (1997).
[13] P. A. Boasman, Nonlinearity **7**, 485 (1994).
[14] E. J. Heller, J. Chem. Phys. **72**, 1337 (1980); E. J. Heller, Phys. Rev. A **35**, 1360 (1987).
[15] E. B. Bogomolny, Nonlinearity **5**, 805 (1992).
[16] S. D. Frischat and E. Doron, J. Phys. A **30**, 3613 (1997).
[17] P. W. O'Connor, S. Tomsovic, and E. J. Heller, Physica D **55**, 340 (1992).